Ambient effects on the output strain of Ni–Mn-Ga single crystal magnetic shape memory alloy

Shaobin Zhang, Guoshun Qin, Yongjun He

HAL Id: hal-03490799
https://hal.science/hal-03490799

Submitted on 20 May 2022

Ambient effects on the output strain of Ni-Mn-Ga single crystal magnetic shape memory alloy

Shaobin Zhang[a], Guoshun Qin[b], Yongjun He[b,*]

[a]*School of Mechanics, Civil Engineering and Architecture,*
Northwestern Polytechnical University, Xi'an, China

[b]*IMSIA, CNRS, EDF, CEA, ENSTA Paris,*
Institut Polytechnique de Paris, Palaiseau Cedex, France

Corresponding author (Yongjun He). Tel.: (+33) 169319730; fax: (+33) 169319997.
E-mail address: yongjun.he@ensta-paristech.fr

Abstract:

With proper magneto-mechanical driving forces (e.g., a high-frequency magnetic field plus a mechanical force), Magnetic Shape Memory Alloy (MSMA) can provide a large cyclic deformation (strain oscillation amplitude up to 6%), which makes it a good candidate for high-frequency large-stroke actuators. Moreover, as a kind of shape memory alloys, MSMA's magneto-mechanical coupling behaviors are very sensitive to temperature, which allows researchers/engineers to modify the strain oscillation amplitude for a wider range of applications by controlling the working temperature. In this paper, we report systematic experiments on the thermal-ambient-dependent oscillation amplitude of the magnetic-field-induced martensite reorientation—utilizing compressed air (with controlled airflow velocity) passing through the surface of the MSMA specimen (Ni-Mn-Ga single crystal) to control the heat transfer between the ambient and the MSMA specimen during the high-frequency magneto-mechanical loading. It is found that the extremely weak or extremely strong ambient heat transfer can only have small strain oscillation amplitude while the maximum strain amplitude can be achieved only at a mild heat-transfer condition (i.e., non-monotonic dependence of the strain amplitude on the ambient heat transfer). It is also demonstrated that the strain amplitude is closely related to the working temperature,

satisfying the balance between the heat generation (from the dissipative strain oscillation of the martensite reorientation) and the heat transfer to ambient (due to the temperature difference between the MSMA specimen and the ambient). With such understanding and constraints, three different schemes for controlling the strain amplitude by the thermal method are proposed and tested for their robustness/reliability. These results not only provide some guidelines/principles for designing MSMA actuators with flexible strain amplitude, but also demonstrate the delicate dynamics of the thermo-magneto-mechanical coupling that demand further theoretical/modelling study.

1. Introduction

Magnetic Shape Memory Alloy (MSMA) is a smart material with multi-physics coupling as demonstrated by the large magnetic-field-induced deformation (up to 10% strain) [1–5]. When the magneto-mechanical driving forces are applied properly (satisfying some criteria [6–11]), large cyclic recoverable deformation can be achieved (so-called superelasticity), making the material a good choice for large-stroke actuators. Particularly, the large amplitude of strain oscillation controlled by high-frequency magnetic field makes MSMA a unique candidate for advanced actuators [12–15] in comparison with other smart materials such as piezoelectric materials, magnetostrictive materials, and traditional shape memory alloys. Several researchers have investigated the performance of the MSMA actuator prototypes and the associated magneto-mechanical governing parameters such as the magneto-mechanical loading frequency [16–19], the applied mechanical stress [20,21], and the system mechanical stiffness [20–22]. In fact, besides these magneto-mechanical boundary conditions in governing the strain oscillation amplitude, there is another important factor: temperature, when we examine the physical mechanisms of the magnetic-field-induced deformation of MSMA[23–25].

The large field-induced deformation of MSMA is caused by either the martensite reorientation with a magnetic field less than 1 Tesla [2,26–28] or the martensitic phase transformation with a strong magnetic field larger than 2 Tesla [26,29]. Due to the advantages of the relatively low loading field and the low hysteresis/dissipation (small twinning stress)[30–32], the martensite reorientation is mainly adopted for the field-induced deformation of MSMA actuators. However, as recent studies revealed [20,21,33–35], although the twinning stress is low (0.2MPa ~ 2MPa), the dissipation heat quickly accumulated during the high-frequency field-induced martensite reorientation can cause a rapid temperature rise in MSMA, even triggering the phase transformation to significantly influence the output strain oscillation amplitude. Moreover, because the twinning stress is sensitive to temperature (particularly Type I twinning stress decreases with increasing temperature) [24], the temperature rise changing the twinning stress (i.e., changing damping capacity) can modify the strain oscillation during the actuation process of MSMA actuators.

In other words, the temperature must be well controlled to achieve a reliable working state (a stable strain oscillation).

The recent experiments [33,34] utilized compressed airflow (controlling the airflow velocity) to pass through the surfaces of the MSMA specimen to tune the ambient heat-transfer condition so to control the working temperature during the high-frequency strain oscillation. It was demonstrated that this thermal method can influence the temperature-govern processes (martensite reorientation and phase transformation) in both the macroscopic behaviors (e.g., modifying the global output strain amplitude) and the microstructure evolution (e.g., redistributing the volume fractions of different phases/variants). However, so far in literature, there is no accurate model for quantitative predictions on these thermo-magneto-mechanical coupling behaviors; even the basic design principles for MSMA actuators are not clear, for example, how to properly set thermal boundary condition to achieve the wanted stable working states?

In this paper, we first report an experiment with gradually changing the ambient heat-transfer condition (from ambient still air to strong ambient airflow) to systematically demonstrate the thermal effects on the strain oscillation and the associated working temperature of a Ni-Mn-Ga single crystal MSMA specimen under high-frequency magneto-mechanical loading. It is found that the extremely weak or the extremely strong ambient heat transfer can only have small strain oscillation amplitude while the maximum strain amplitude can be achieved only at a mild heat-transfer condition (i.e., non-monotonic dependence of the strain amplitude on the ambient heat transfer). It is also demonstrated in this experiment that the strain amplitude can be changed significantly (from less than 2% strain amplitude to near theoretical maximum value 6% of the full martensite reorientation) and the working temperature is closely related to the strain oscillation amplitude, which together satisfy the balance between the heat generation (from the dissipative strain oscillation of the martensite reorientation) and the heat transfer to ambient (due to the temperature difference between the MSMA specimen and the ambient). Further, we perform another set of experiments with switching between two significantly different thermal conditions (i.e., the ambient airflow velocity changes largely and rapidly) to verify the robustness/reliability of the

dynamic transition between different working states. It was revealed that three qualitatively different types/schemes of the dynamic transitions can be identified, according to the participation and the relative importance of the two physical mechanisms in the dynamic transition (i.e., the temperature-dependent martensite reorientation and the temperature-induced phase transformation). Based on these dynamic experiments, some guidelines/principles of the thermal method for controlling the magnetic-field-induced strain amplitude are summarized and some challenging theoretical/modelling issues about the complicated multi-physics coupling dynamics are pointed out.

The remaining parts of this paper are organized as the following. Section 2 describes the material properties and the experimental setup for current experiments. Section 3 reports the results of the two sets of experiments (gradual transition and rapid/dynamic transition) and the associated theoretical thermal analysis and discussion. Finally, a summary is given in Section 4.

2. Material properties and Experiment setup

A $Ni_{50}Mn_{28}Ga_{22}$ (at. %) single crystal MSMA specimen (from ETO Magnetic GmbH) was used in the experiments of this study. The specimen was cut to a rectangular bar with all faces of the specimen parallel to the {100} planes of the parent cubic austenite (with a lattice parameter of a_0). The total length of the specimen L_{total} is 13 mm and the sectional area is 5×2 mm. The specimen is in the state of 10M martensite phase at room temperature. Note that the martensite variants are slightly monoclinic in this material, but in this work it is assumed that they are tetragonal with two long axes "a" and one short axis "c" for the simplicity of the analysis. The material characteristic phase transformation temperatures M_s, M_f, A_s and A_f were obtained as 38.6 °C, 36.3 °C, 44.8 °C, and 46.8 °C respectively from a DSC test (differential scanning calorimetry).

To experimentally investigate the MSMA actuator performances, a thermo-magneto-mechanical loading system is developed as shown in Fig. 1(a). Before each test, the martensite specimen is fully compressed along y-axis (by applying a large mechanical compression stress, larger than 10 MPa) to obtain a single variant state with the short-axis

(c-axis) along y-direction (so-called stress-preferred variant, shown as M_1 in Fig. 1(b)), so that all the tests can take the same reference state (i.e., zero strain) for calculations of the specimen's deformation strain in this work. The specimen is installed between two magnetic poles with the long side along y-direction by two lightweight plexiglass holders. At the beginning of each test, an initial compressive stress σ_{ini} is applied on the single-martensite-variant specimen along y-direction by a compressed spring. Then a magnetic field of frequency f_{mag} (with magnetic flux density $\boldsymbol{B}$ cyclically varying between [-0.78, 0.78] Tesla in a triangular waveform) is applied horizontally by the electro-magnet to drive the martensite reorientation from M_1 to M_2 (so-called magnetic-field-preferred variant with the short axis along x-direction and the long axis a along y-direction) as shown in Fig. 1(b). During this martensite reorientation process, the length of the specimen gauge-section L_{gauge} (the gauge section is the part of the specimen between the upper and lower holders/clampers, initially L_{gauge} = 6.7 mm) changes due to the microscopic difference between the lattice parameters of M_1 and M_2 along y-direction (i.e., the difference between the long and short axes, a and c), which causes the change in the spring length so that the spring compressive stress along y-direction changes at the same time. Thus, the interaction between the cyclic magnetic field (along x-direction) and the correspondingly evolving compressive stress (from the spring along y-direction) eventually leads to a cyclic deformation strain of MSMA (by cyclic martensite reorientation between the variants M_1 and M_2). In this experimental system, during the magneto-mechanical cyclic loading, the ambient heat-transfer efficiency of the MSMA specimen can be controlled by applying an ambient airflow of different velocities to pass through the specimen surfaces.

During the actuation, the deformation of the specimen along y-direction is measured by a laser displacement sensor (Keyence LK-H027) at the upper holder, and the average temperature of the specimen is monitored by a thermocouple (K-type, 0.5 mm sheath diameter) at bottom of the specimen. Because the specimen holders are made of plexiglass of low thermal conductivity to reduce the heat conduction from the specimen ends to the fixtures, it is assumed that the heat convection via the specimen surface is the dominant path of the heat exchange rather than the heat conduction via the specimen ends. The heat-transfer

efficiency can be quantified by a characteristic heat relaxation time t_h which depends on the ambient airflow velocity (the details about the measurement of t_h can be found in Appendix A). That means, a large airflow velocity leads to a high heat-transfer efficiency corresponding to a short characteristic heat relaxation time t_h.

3. Experimental results and discussions

This section is divided into three subsections. In order to demonstrate the thermal effect on the magnetic-field-induced strain oscillation in MSMA, a test of high-frequency magnetic actuation with stepwise increasing heat-transfer efficiency (increasing the velocity of ambient airflow) is reported in Subsection 3.1. To understand the physical mechanisms and the associated governing parameters on the thermal effect, a simple thermal analysis considering the heat balance is conducted in Subsection 3.2. Finally, based on the understanding, we design and test three typical schemes to control the output strain amplitude in Subsection 3.3, as examples to demonstrate the reliable thermal method to control the strain oscillation.

3.1 Ambient heat-transfer effect on magnetic-field-induced strain oscillation

To investigate the heat-transfer effect on the MSMA's high-frequency strain amplitude, a magnetic actuation test is conducted under a stepwise increasing heat-transfer efficiency (applying an airflow passing through the specimen with gradually increasing velocity in several small steps). The frequency of the applied magnetic field (f_{mag}) is 110 Hz (accordingly the strain oscillation frequency $f_{strain} = 2\ f_{mag} = 220$ Hz), and the applied initial compressive stress (σ_{ini}) is 0.4 MPa. The strain and the temperature evolutions of the MSMA are shown in Fig. 2(a) and the magnified views on the strain oscillation curves at some typical time instants are shown in Fig. 2(b). It is seen that, at the beginning of the actuation (< 26 seconds) where the specimen is in the still air ambient (whose characteristic heat relaxation time t_h is 80.0 seconds as measured in Appendix A), a large strain amplitude $\Delta\varepsilon$ around 6% (the strain difference between the maximum and the minimum nominal strains) can be obtained. At the same time, the specimen temperature increases from the room temperature (around 20 °C) to 37.8 °C which is within the range of the martensitic phase transformation (i.e., 36.3 °C = M_f < $T_{specimen}$ < A_f = 46.8 °C). Then, at around $t \approx 27$ s, a significant reduction in the strain

amplitude occurs: $\Delta\varepsilon$ decreases from 6% to around 1.9%. This sudden strain reduction (so-called strain drop marked by a red arrow in Fig. 2(a)) is caused by the Martensite-to-Austenite phase transformation induced by the temperature rise; with the in-situ observation on the specimen surface by an optical camera, we can see the appearance of a large non-active zone (of Austenite phase which doesn't provide any cyclic deformation in such magnetic field) as shown in the schematics in Fig 2(b) at the time instant $t_1 \approx 40$ s. Detailed verification, analysis, and discussion on the M→A phase transformation during the magnetic-field induced martensite reorientation can be found in our previous studies [33–35]. After the strain drop, both the output strain amplitude $\Delta\varepsilon$ and the specimen temperature T reach stable states with the strain amplitude of 1.9% and the temperature of 37.8 °C as shown in the evolutions at the time instant t_1 in Fig. 2; particularly, it is seen in the schematics of Fig. 2(b) about the phase/variant distributions at the instant t_1 that only a part of the specimen cyclic changes between the M_1 and M_2 martensite variants during the cyclic magnetic field loading, while the rest part is Austenite (non-active zone). In other words, during the strain drop, the specimen self-organizes its microstructure into different parts: the active part (providing cyclic deformation) and the non-active part (without contribution to output strain amplitude). The reason for such self-organization and the mechanisms determining the volume fractions of the different parts will become clear in the following further tests and the analysis in Subsection 3.2.

As shown in Fig. 2(a), when the characteristic heat relaxation time t_h is stepwise decreased from 80.0 s to 14.9 s (at the time instant t_3), the strain amplitude increases stepwise from 1.9% to 5.6%, nearly reaching the theoretically maximum strain amplitude (6%); at the same time the stepwise temperature change is slight (only 1.1 °C reduction from the instant t_1 to t_3 in Fig. 2(a)). Such thermal effect on the output strain amplitude can be understood by the schematics of the evolutions of the phase/variants at the peak and valley of the deformation cycles (strain oscillations) at some typical instants (t_1~t_5) in Fig. 2(b). For example, in comparison of the phase/variant distributions between the instants t_1 and t_2, the volume of the non-active Austenite zone is smaller at t_2; that is why the output strain amplitude becomes larger at t_2 (larger Martensite active zone taking cyclic reorientation between variants M_1 and

M$_2$)—the higher efficiency (shorter t_h) of the heat-transfer to ambient allows more dissipative Martensite reorientation process. Another key point is the slight temperature change: 37.8 °C to 37.3 °C from t_1 to t_2; both the temperature levels are within the range of the martensitic phase transformation, $M_f < T_{specimen} < A_f$, which allows the coexistence of both phases: Martensite and Austenite. In other words, according to the heat-transfer condition (the level of t_h), the MSMA specimen adjusts its volume fractions of the two phases (the non-active Austenite without local strain oscillation and the active Martensite with 6% local strain oscillation amplitude) for the balance between the dissipation heat generated by the dissipative martensite reorientation (dissipative strain oscillation) and the heat transfer to ambient due to the temperature difference between the specimen and the ambient.

When the ambient heat-transfer efficiency is high enough (i.e., t_h is short enough) as at the instant t_3 in Fig. 2, the specimen is almost fully transformed into Martensite which takes a complete cyclic reorientation between M$_1$ and M$_2$ to provide a large output nominal strain amplitude of 5.6%. However, when the heat relaxation time t_h is further stepwise decreased to 8.0 s (at the time instant t_5), both the strain amplitude and the temperature decrease significantly as shown in Fig. 2(a), where $\Delta\varepsilon = 2.1\%$ and $T_{specimen} = 22.0$ °C. This thermal effect on the strain amplitude is due to the temperature dependence of the martensite reorientation process: when the ambient heat-transfer is strong (stronger than the dissipation heat generation of the martensite reorientation), the specimen temperature decreases significantly below M_f (e.g., $T = 26.4$ °C at t_4), making the martensite reorientation more difficult to proceed because the dissipative force (resistant force, so-called twinning stress) of the martensite reorientation increases with decreasing temperature as experimentally investigated in literature [24,36]. In other words, the higher damping (higher dissipation) in the dynamic oscillating system leads to the lower output oscillation amplitude. In this case, even though the specimen is fully occupied by Martensite in the low temperature (lower than M_f), not all the Martensite zones are active. As shown in the schematics of t_4 and t_5 in Fig. 2(b), some Martensite zones are non-active, always staying in the state of M$_1$ or M$_2$, without local strain oscillation. In comparison between the time instants t_4 and t_5, we can see that the

output strain amplitude decreases from 3.2% to 2.1% with the increase in the volume fraction of the non-active Martensite zones.

The above thermal effects on the strain oscillation amplitude and the associated temperature are summarized in Fig. 3 which indicates the dependence of the step-stable strain oscillation amplitude and the associated temperature on the characteristic heat relaxation time t_h. It is seen that, with decreasing t_h (i.e., increasing ambient airflow velocity), the stable strain amplitude $\Delta\varepsilon_{stable}$ changes non-monotonically while the stable temperature T_{stable} decreases monotonically. The maximum output strain is obtained at around $t_h = 14.9$ s where the temperature starts to decrease below M_f. That means, to achieve the maximum output strain amplitude, a proper ambient heat-transfer condition is needed to tune the specimen working temperature close to (but lower than) the phase transformation temperature (M_f) so that the whole specimen is occupied by Martensite phase and the temperature-dependent twinning stress (dissipative force) is relatively low.

Taking the optimal t_h (=14.9 s for the maximum $\Delta\varepsilon_{stable}$) as a reference point, Figure 3 clearly indicates two different regions of the thermal effect: weak heat-transfer condition ($t_h >$ 14.9 s) and the strong heat-transfer condition ($t_h <$ 14.9 s). In the region of weak heat transfer, the temperature is always within the range of the phase transformation temperatures ($M_f <$ $T_{specimen} < M_s$), the strain amplitude is modified mainly by the self-adjustment of the volume fractions of the active Martensite and the non-active Austenite via the A↔M phase transformation. By contrast, in the region of strong heat transfer, the specimen temperature is below M_f and the amplitude change is due to the temperature dependence of the dissipative resistant force (twinning stress) of the martensite reorientation. Therefore, the overall thermal effect on the strain amplitude is due to two mechanisms (the phase-fraction adjustment and the temperature dependence of twinning stress) whose contributions and relative importance depend on the specimen working temperature (above or below M_f). Nevertheless, the strain amplitude change by the two mechanisms of the thermal effect needs to satisfy the heat balance: the balance between the dissipation heat generated by the dissipative martensite

reorientation and the heat transfer to ambient, which are quantified and discussed in next subsection.

3.2 Simple thermal analysis

The heat balance of shape-memory-alloy structures has been well studied in literature [33,37–39], based on which a simple thermal model for current MSMA system can be obtained as the following (detailed derivation can be found in Appendix B):

$$\frac{dT}{dt} = \frac{q_{Dissipation} - q_{Transfer}}{\lambda} \tag{1a}$$

where

$$q_{Dissipation} = 2\sigma_{tw} \cdot \Delta\varepsilon_{stable} \cdot f_{strain} \tag{1b}$$

$$q_{Transfer} = \frac{(T - T_0) \cdot \lambda}{t_h} \tag{1c}$$

Equation (1a) means that the changing rate of the specimen temperature (T) is proportional to the net heating rate (the difference between the dissipation heat generation rate $q_{Dissipation}$ and the ambient heat-transfer rate $q_{Transfer}$ (unit: J·m^{-3}·s^{-1})) and is inversely proportional to the material's specific heat λ (unit: J·m^{-3}·K^{-1}); Eq. (1b) indicates that the dissipation heat generation rate $q_{Dissipation}$ due to the martensite reorientation is 2 times the product of the twinning stress σ_{tw}, the strain amplitude $\Delta\varepsilon$ in one oscillation cycle and the frequency of the strain oscillation (i.e., the number of the actuation cycles per second); Eq. (1c) shows that the ambient heat-transfer rate $q_{Transfer}$ is proportional to the material's specific heat and the temperature difference between the specimen (T) and the ambient (T_0), and is inversely proportional to the characteristic heat relaxation time t_h.

It is seen from Eq. (1a) that, when $q_{Dissipation} > q_{Transfer}$ (or $q_{Dissipation} < q_{Transfer}$), the specimen temperature T increases (or decreases). Only when $q_{Dissipation} = q_{Transfer}$, the system reaches stable states, i.e.,

$$2\sigma_{tw} \cdot \Delta\varepsilon_{stable} \cdot f_{strain} = q_{Dissipation} = q_{Transfer} = \frac{(T_{stable} - T_0) \cdot \lambda}{t_h} \tag{2}$$

In Eq. (2), all the parameters at the most right-hand and the most left-hand sides can be directly measured except the twinning stress σ_{tw}. According to the previous studies in literature [4, 14, 15, 22], the martensite reorientation occurs via the motion of the twin boundaries of two different types (so-called Type I and Type II) with different twinning stresses denoted by σ_{tw}^{I} and σ_{tw}^{II}, among which, only σ_{tw}^{I} depends on temperature [24]:

$$\sigma_{tw}^{I} \approx 0.2 - 0.04 \cdot (T - As) \qquad MPa \tag{3a}$$

$$\sigma_{tw}^{II} \approx 0.2 \qquad MPa \tag{3b}$$

where A_s denotes the austenite starting temperature of the phase transformation. Our previous study [21,40] demonstrated that both types of twin boundary motions contribute to the MSMA dynamic deformation; so the effective twinning stress σ_{tw} should include the contributions of both σ_{tw}^{I} and σ_{tw}^{II} as:

$$\sigma_{tw} = v \cdot \sigma_{tw}^{I} + (1 - v) \cdot \sigma_{tw}^{II} \tag{4}$$

where v denotes the fraction of Type I twin boundary motion contributing to the dynamic deformation. As Type II twin boundary motion is easier than Type I twin and plays a more important role in the temperature rise of the dynamic actuation [40], v is assumed to be a small value here ($v = 0.1$). Therefore, combining Eqs. (3) and (4) and the measurable parameters/variables ($\Delta\varepsilon_{stable}$, T_{stable}, T_0, λ, f_{strain}, and t_h.), we can quantify the step-stable rates of the dissipation heat generation and the ambient heat transfer to verify the heat balance of Eq. (2) as shown in Fig. 4(a). It is seen that the heat balance is satisfied quite well, keeping in mind that there might be some errors in the temperature measurement as the temperature sensor (thermocouple) is attached at the specimen's end rather than direct contact to the gauge section (the middle part of the specimen), and that some minor heat generation due to eddy

current generated by high-frequency magnetic field has been ignored, which were experimentally measured and discussed in literature [20,33].

So, we can utilize this balance equation to estimate strain amplitude control, such as the relation between the strain amplitude $\Delta\varepsilon$, working temperature T and the characteristic heat relaxation time t_h. For example, in the region of weak heat transfer ($t_h > 14.9$ s) in Fig. 3, the specimen temperature is very close to M_f, i.e.,

$$T_{stable} \approx M_f \tag{5}$$

Combining Eqs. (2) ~ (5), we have

$$\Delta\varepsilon_{stable} = C \cdot \frac{1}{t_h} \tag{6}$$

where

$$C = \frac{(M_f - T_0) \cdot \lambda}{2 f_{strain} \cdot [0.2 - 0.04 \cdot v \cdot (M_f - A_s)]}.$$

Equation (6) of the simple inversely proportional relation well captures the t_h-dependence of the strain amplitude as shown in Fig. 4(b).

However, it is noted that the heat balance equation (Eq. (2)) alone can't predict the two response variables (T_{stable} and $\Delta\varepsilon_{stable}$) without a mechanical force balance equation considering the magneto-mechanical driving forces and the dynamic inertial effect. So, a complete model on the dynamic strain oscillation of the MSMA is still demanded and it is a challenging task involving the complicated non-smooth processes, such as the martensite reorientation with dissipative twinning stress (like dry friction) and the A-M phase transformation with thermo-mechanical coupling. Nevertheless, the heat balance equation is helpful in understanding the thermal effects, particularly the relation between T_{stable} and $\Delta\varepsilon_{stable}$ as shown in Fig. 5 which is discussed and utilized to design some reliable schemes/methods for controlling the strain amplitude in the next subsection.

3.3 Typical schemes for controlling strain amplitude

Based on the summarized thermal effect in Fig. 3, we can plot Fig. 5 to show the MSMA's working states (the stable strain amplitude and the corresponding working temperature) under the given magneto-mechanical loading (whose key parameters f_{mag} =110 Hz and σ_{ini} = 0.4 MPa in the current test). Fig. 5 implies that the output strain amplitude $\Delta\varepsilon$ can vary in a wide range from a small value (near 0%) to near the theoretical maximum value of martensite reorientation (close to 6%), and the working temperature T is within the range from T_0 (the ambient airflow temperature around 18 °C) to the material characteristic temperature M_s of the martensitic phase transformation. But MSMA can't work at all arbitrary combinations of $\Delta\varepsilon$ and T, i.e., the working state must satisfy certain relations between $\Delta\varepsilon$ and T. For example, when $T < M_f$, the strain amplitude $\Delta\varepsilon$ significantly increases with increasing temperature T because the dissipative twinning stress (resistant force) decreases with increasing T (and no phase transformation involvement below M_f). By contrast, when the temperature is above M_f, the strain amplitude change is accompanied with only slight temperature change via the phase-fraction adjustment by phase transformation (note: theoretically, the martensite volume fraction can change from 0% to 100% for the martensitic phase transformation within the small temperature difference M_s - M_f = 38.6 °C - 36.3 °C = 2.3 °C like in the DSC test). Therefore, by proper ambient airflow control (changing t_h), the output strain amplitude can be changed from 0% to 6% at both the temperature ranges, [T_0, M_f] and [M_f, M_s]. In other words, for achieving a certain strain amplitude, there exist two possible working temperature levels, each within one of the two temperature ranges [T_0, M_f] and [M_f, M_s], which can be approximately described by the following two equations:

$$\Delta\varepsilon = -0.01T^2 + 0.89T - 12.91 \qquad \text{where } T_0 < T < M_f, \qquad (7a)$$

$$\frac{(M_s - T)}{0\% - \Delta\varepsilon} = \frac{(M_s - M_f)}{0\% - 6\%} \rightarrow \Delta\varepsilon = 6\% \cdot \frac{(M_s - T)}{(M_s - M_f)} \qquad \text{where } M_s > T > M_f, \qquad (7b)$$

where Eq. (7a) is determined by data fitting (to a quadratic equation) and Eq. (7b) is a linear dependence of the strain amplitude on the temperature between M_s and M_f. So, combining the

above two equations (Eqs. (7a) and (7b)) and the heat balance equation Eq. (2), we can design a working state (i.e., choosing a combination of T and $\Delta\varepsilon$) and determine the setting of a proper heat-transfer condition (the level of t_h) to achieve the designed working state. The tests in Fig. 2 have already demonstrated the successful strain amplitude control with gradually tuning t_h (see the data of blue solid circles in Fig. 5). But, in most advanced engineering applications, it might be demanded to change from one working state to another rapidly and reliably. To verify the robustness of the strain amplitude control of the system, we perform new tests by changing t_h suddenly (i.e. changing the airflow velocity rapidly, with the operation time less than 2 seconds) as shown in Fig. 6 where three typical tests demonstrate the system switch between two working states by cyclically controlling the level of t_h.

As discussed in Eq. (7a) and (7b), there are two temperature ranges (two relations between the strain amplitude $\Delta\varepsilon$ and temperature T) which are governed by two different physical mechanisms (temperature-dependent dissipative twinning stress and the phase-fraction adjustment). So, basically we have three different schemes for a given strain amplitude switching (for example, switching between $\Delta\varepsilon_1$ and $\Delta\varepsilon_2$); in other words, we can choose different working temperatures for the transition between two stable working states S_1 (consisting of T_1 and $\Delta\varepsilon_1$) and S_2 (consisting of T_2 and $\Delta\varepsilon_2$). As indicated by the three solid arrowed curves in Fig. 5, we have three qualitatively different settings: (I) let both T_1 and T_2 be less than M_f, setting both T_1 and T_2 according to Eq. (7a), i.e., with two different levels of strong airflow (short t_h) for the two working states; (II) let both T_1 and T_2 be higher than M_f, setting both T_1 and T_2 according to Eq. (7b), i.e., with two different levels of weak airflow (large t_h) for the two working states; (III) let T_1 and T_2 be in different temperature ranges (e.g., $T_1 < M_f$ and $T_2 > M_f$). The three schemes have different dynamic transition features as shown in Figs. 6(a), (b) and (c), respectively.

In Fig. 6(a) of the scheme (I) with cyclic changing t_h between 10.5 s and 8.0 s, the stable strain amplitude switches between around 4.7% and around 2.4% while the two stable working temperatures are around 30 °C and 24 °C which are significantly less than M_f to avoid the participation of Austenite. The two stable working states, S_1 = (~4.7%, ~30 °C) and

$S_2 = (\sim2.4\%, \sim24\ °C)$ satisfy the relation of Eq. 7(a) as shown in Fig. 5 (see the data of green squares). As the temperature dependence of the resistant twinning stress governs this strain amplitude change, the working-state dynamic transition mainly depends on the temperature difference between T_1 and T_2 (here $\Delta T \approx 6\ °C$) during the controlled heat transfer (particularly controlled by t_h). It is seen in Fig. 6(a) and Table 1 that the time of the transition from S_1 to S_2 is around 20 s (e.g., $t_1^{trans} = t_1^{stable} - t_1^{switch} \approx 19$ s for the transition during the ambient heat transfer of $t_h = 8.0$ s), while the time of the reverse transition from S_2 to S_1 is around 50 s (e.g., $t_2^{trans} = t_2^{stable} - t_2^{switch} \approx 53$ s for the transition during $t_h = 10.5$ s); in other words, the longer the t_h of the ambient heat transfer, the longer the state transition time. And the transition time is larger than its corresponding t_h in current test.

In Fig. 6(b) of the scheme (II) with cyclic changing t_h between 80.0 s and 25.0 s, the system switches between the two states: $S_1 = (\sim2.2\%, T_1 \approx M_f)$ and $S_2 = (\sim4.1\%, T_2 \approx M_f)$ as summarized in Fig. 5 (see the data of black triangles)—there are scattering/errors in the temperature measurements on T_1 and T_2, the reason might be that the dynamic-changing active zones at the specimen's gauge section are not directly measured/contacted by the sensor/thermocouple which is attached at the end of the specimen. As the temperature change (the difference between T_1 and T_2) is not large, both the forward (S_1 to S_2) and the reverse (S_2 to S_1) transition times are small (around 12 s and 9 s respectively) and much less than the corresponding t_h.

In Fig. 6(c) of the scheme (III) with cyclic changing t_h between 80.0 s and 10.0 s, the system switches between the two states: $S_1 = (\sim2.4\%, T_1 \approx M_f)$ and $S_2 = (\sim3.4\%, T_2 \approx 25.8\ °C < M_f)$. Different from the schemes (I) and (II) whose transition between two stable strain amplitudes is smooth (monotonic), the scheme (III) has a non-monotonical change in the strain amplitude during the transition—the strain amplitude passes the maximum martensite-reorientation value (6%) during the switch between S_1 and S_2. More interestingly, the forward transition time from S_1 to S_2 is much longer than that of the reverse transition from S_2 to S_1, e.g., $t_1^{trans} \approx 82s$ significantly larger than $t_2^{trans} \approx 20s$. Such complicated dynamic transition features are attributed to the coupling of the two mechanisms (the

temperature-dependence of the twinning stress and the phase-fraction adjustment). Full understanding and quantitative prediction on such transition phenomena demand advanced dynamic models for the thermo-magneto-mechanical coupling behaviors.

Comparing the performances of these three schemes in Table 1 about the transition times and in Fig. 7 about the data scattering of the controlled strain amplitudes, we can see that Scheme (II) has the fastest response/transition and small scattering in the strain amplitudes, but it has a limited range of the working temperature related to the material's characteristic phase transformation temperature (M_f and M_s). By contrast, Scheme (I) has a wider working temperature range (from T_0 to M_f) while its scattering in strain amplitude is small; moreover, there is no austenite participation in Scheme (I) making the microstructure avoid the complex A-M interface and the compatibility problem, which might influence the material's fatigue behavior. Normally, Scheme (III) would not be suggested for engineering applications because it has non-smooth strain amplitude change (always passing a peak strain amplitude 6% during the transition) and the transition time is the longest among the three schemes.

4. **Summary**

In this paper, the thermal effect on the magnetic-field-induced strain oscillation of magnetic shape memory alloy is investigated by the systematic experiments with stepwise gradually changing thermal boundary condition (from still ambient air to strong airflow) and the dynamic experiments of cyclic rapid switching between different levels of the ambient heat-transfer efficiency (characterized the heat relaxation time t_h). There are abundant interesting phenomena, such as the *non-monotonic t_h*-dependence of the strain oscillation amplitude (Fig. 3), the *inverse proportional* relation between the strain amplitude and t_h in the region of weak heat transfer (Fig. 4(b)), and the necessary passage through the maximum strain amplitude (6%) during the state transition crossing the critical temperature M_f (see Scheme (III) in Fig. 5 and Fig. 6(c)). All these phenomena can be basically understood with the two physical mechanisms: the temperature dependence of the martensite-reorientation resistant force (twinning stress) and the phase-fraction adjustment of the martensitic phase transformation. As the two mechanisms involve non-smooth processes of multi-physics

coupling, advanced models (with quantitative prediction and/or detailed simulation) are demanded for both fundamental understanding and engineering designs.

This work is focused on the thermal method to control the strain oscillation amplitude of magnetic-field-induced martensite reorientation of MSMA, studying the MSMA performance under a given magneto-mechanical loading. It is expected that different magneto-mechanical loadings (e.g., changing the frequency) would change the strain amplitude. But the qualitative features of the thermal methods (e.g., the dynamic transition features of Schemes I, II and III in Figs. 5 and 6) would be the same, while quantitative changes are anticipated, e.g., the maximum strain amplitude of the necessary passage of Scheme III might be less than 6% if the magneto-mechanical forces do not allow full martensite reorientation. To provide a full picture of the system performance under various thermo-magneto-mechanical loadings, more careful experiments are needed in the future.

References

[1]   K. Haldar, D.C. Lagoudas, Dynamic magnetic shape memory alloys responses: Eddy current effect and Joule heating, J. Magn. Magn. Mater. 465 (2018) 278–289. doi:10.1016/j.jmmm.2018.05.107.

[2]   S.J. Murray, M. Marioni, S.M. Allen, R.C. O'Handley, T.A. Lograsso, 6% magnetic-field-induced strain by twin-boundary motion in ferromagnetic Ni–Mn–Ga, Appl. Phys. Lett. 77 (2000) 886–888. doi:10.1063/1.1306635.

[3]   E. Pagounis, R. Chulist, M.J. Szczerba, M. Laufenberg, Over 7% magnetic field-induced strain in a Ni-Mn-Ga five-layered martensite, Appl. Phys. Lett. 105 (2014) 1–5. doi:10.1063/1.4892633.

[4]   P. Cejpek, L. Straka, M. Veis, R. Colman, M. Dopita, V. Holý, O. Heczko, Rapid floating zone growth of Ni2MnGa single crystals exhibiting magnetic shape memory functionality, J. Alloys Compd. 775 (2019) 533–541. doi:10.1016/j.jallcom.2018.10.113.

[5] M.F. Qian, X.X. Zhang, C. Witherspoon, J.F. Sun, P. Müllner, Superelasticity and shape memory effects in polycrystalline Ni–Mn–Ga microwires, J. Alloys Compd. 577 (2013) S296--S299. doi:10.1016/j.jallcom.2011.10.117.

[6] X. Chen, Y. He, Z. Moumni, Twin boundary motion in NiMnGa single crystals under biaxial compression, Mater. Lett. 90 (2013) 72–75. doi:10.1016/j.matlet.2012.08.107.

[7] Y.J. He, X. Chen, Z. Moumni, Two-dimensional analysis to improve the output stress in ferromagnetic shape memory alloys, J. Appl. Phys. 110 (2011) 1–11. doi:10.1063/1.3636366.

[8] Y.J. He, X. Chen, Z. Moumni, Reversible-strain criteria of ferromagnetic shape memory alloys under cyclic 3D magneto-mechanical loadings, J. Appl. Phys. 112 (2012) 33902. doi:10.1063/1.4739711.

[9] J. Wang, P. Du, Theoretical study and numerical simulations on the stress-induced twin interface nucleation in single-crystalline NiMnGa alloys, J. Appl. Phys. 126 (2019). doi:10.1063/1.5115486.

[10] O. Heczko, L. Straka, I. Aaltio, S.P. Hannula, Strain and concurrent magnetization changes in magnetic shape memory Ni-Mn-Ga single crystals - experiment and model, Mater. Sci. Eng. A. 481–482 (2008) 283–287. doi:10.1016/j.msea.2006.12.236.

[11] H. Seiner, L. Straka, O. Heczko, A microstructural model of motion of macro-twin interfaces in Ni–Mn–Ga 10M martensite, J. Mech. Phys. Solids. 64 (2014) 198–211. doi:10.1016/j.jmps.2013.11.004.

[12] R. Yin, F. Wendler, B. Krevet, M. Kohl, A magnetic shape memory microactuator with intrinsic position sensing, Sensors Actuators, A Phys. 246 (2016) 48–57. doi:10.1016/j.sna.2016.05.013.

[13] E. Pagounis, R. Chulist, M.J. Szczerba, M. Laufenberg, High-temperature magnetic shape memory actuation in a Ni–Mn–Ga single crystal, Scr. Mater. 83 (2014) 29–32. doi:10.1016/j.scriptamat.2014.04.001.

[14] M. Kohl, M. Schmitt, A. Backen, L. Schultz, B. Krevet, S. Fähler, Ni-Mn-Ga shape memory nanoactuation, Appl. Phys. Lett. 104 (2014) 43111. doi:10.1063/1.4863667.

[15] R. Techapiesancharoenkij, J. Kostamo, S.M. Allen, R.C. O'Handley, Frequency response of acoustic-assisted Ni-Mn-Ga ferromagnetic-shape- memory-alloy actuator, J. Appl. Phys. 105 (2009). doi:10.1063/1.3125307.

[16] C.P. Henry, D. Bono, J. Feuchtwanger, S.M. Allen, R.C. O'Handley, ac field-induced actuation of single crystal Ni–Mn–Ga, J. Appl. Phys. 91 (2002) 7810. doi:10.1063/1.1449441.

[17] R. Techapiesancharoenkij, J. Simon, D. Bono, S.M. Allen, R.C. O'Handley, Acoustic-assist effect on magnetic threshold field and twinning-yield stress of Ni-Mn-Ga single crystals, J. Appl. Phys. 104 (2008) 33907. doi:10.1063/1.2961331.

[18] R. Techapiesancharoenkij, J. Kostamo, S.M. Allen, R.C. O'Handley, Frequency response of acoustic-assisted Ni–Mn–Ga ferromagnetic-shape-memory-alloy actuator, J. Appl. Phys. 105 (2009) 93923. doi:10.1063/1.3125307.

[19] M. Mahendran, J. Feuchtwanger, R. Techapiesancharoenkij, D. Bono, R.C.O. Handley, Acoustic energy absorption in Ni-Mn-Ga/polymer composites, J. Magn. Magn. Mater. 323 (2011) 1098–1100. doi:10.1016/j.jmmm.2010.12.025.

[20]   O. Pascan, Y. He, Z. Moumni, W. Zhang, High-frequency performance of Ferromagnetic Shape Memory Alloys, Ann. Solid Struct. Mech. 8 (2016) 17–25.

[21]   O.-Z. Pascan, Dynamic behaviors of Ferromagnetic Shape Memory Alloys, PhD thesis, ENSTA-ParisTech, France, 2015.

[22]   R. Techapiesancharoenkij, The effect of magnetic stress and stiffness modulus on resonant characteristics of Ni–Mn–Ga ferromagnetic shape memory alloy actuators, J. Magn. Magn. Mater. 323 (2011) 3109–3116. doi:10.1016/j.jmmm.2011.06.066.

[23]   N. Okamoto, T. Fukuda, T. Kakeshita, Temperature dependence of rearrangement of martensite variants by magnetic field in 10M, 14M and 2M martensites of Ni-Mn-Ga alloys, Mater. Sci. Eng. A. 481–482 (2008) 306–309. doi:10.1016/j.msea.2006.12.218.

[24]   L. Straka, A. Soroka, H. Seiner, H. Hänninen, A. Sozinov, Temperature dependence of twinning stress of Type I and Type II twins in 10M modulated Ni-Mn-Ga martensite, Scr. Mater. 67 (2012) 25–28. doi:10.1016/j.scriptamat.2012.03.012.

[25]   N. Zreihan, E. Faran, D. Shilo, The effects of temperature on the lattice barrier for twin wall motion, Appl. Phys. Lett. 041605 (2016). doi:10.1063/1.4927660.

[26]   K. Haldar, D.C. Lagoudas, I. Karaman, Magnetic field-induced martensitic phase transformation in magnetic shape memory alloys: Modeling and experiments, J. Mech. Phys. Solids. 69 (2014) 33–66. doi:10.1016/j.jmps.2014.04.011.

[27]   K. Ullakko, J.K. Huang, C. Kantner, R.C. O'Handley, V. V. Kokorin, Large magnetic-field-induced strains in Ni2MnGa single crystals, Appl. Phys. Lett. 69 (1996) 1966–1968. doi:10.1063/1.117637.

[28]   V. Pinneker, R. Yin, C. Eberl, A. Sozinov, Y. Ezer, M. Kohl, Evolution of local strain bands of different orientation in single crystalline Ni-Mn-Ga foils under tension, J. Alloys Compd. 577 (2013) S358--S361. doi:10.1016/j.jallcom.2012.03.004.

[29]   H.E. Karaca, I. Karaman, B. Basaran, D.C. Lagoudas, Y.I. Chumlyakov, H.J. Maier, On the stress-assisted magnetic-field-induced phase transformation in Ni2MnGa ferromagnetic shape memory alloys, Acta Mater. 55 (2007) 4253–4269. doi:10.1016/j.actamat.2007.03.025.

[30]   N. Zreihan, E. Faran, D. Shilo, The effect of loading rate on characteristics of type II twin boundary motion in Ni-Mn-Ga, Scr. Mater. 144 (2018) 44–47. doi:10.1016/j.scriptamat.2017.09.045.

[31]   E. Faran, D. Shilo, Twin motion faster than the speed of sound, Phys. Rev. Lett. 104 (2010) 1–4. doi:10.1103/PhysRevLett.104.155501.

[32]   L. Straka, O. Heczko, H. Seiner, N. Lanska, J. Drahokoupil, A. Soroka, S. Fähler, H. Hänninen, A. Sozinov, Highly mobile twinned interface in 10M modulated Ni–Mn–Ga martensite: Analysis beyond the tetragonal approximation of lattice, Acta Mater. 59 (2011) 7450–7463. doi:10.1016/j.actamat.2011.09.020.

[33]   S. Zhang, X. Chen, Z. Moumni, Y. He, Thermal effects on high-frequency magnetic-field-induced martensite reorientation in ferromagnetic shape memory alloys: An experimental and theoretical investigation, Int. J. Plast. 108 (2018) 1–20. doi:10.1016/j.ijplas.2018.04.008.

[34] S. Zhang, X. Chen, Z. Moumni, Y. He, Coexistence and compatibility of martensite reorientation and phase transformation in high-frequency magnetic-field-induced deformation of Ni-Mn-Ga single crystal, Int. J. Plast. 110 (2018) 110–122. doi:10.1016/j.ijplas.2018.06.010.

[35] X. Chen, Y. He, Thermo-magneto-mechanical coupling dynamics of magnetic shape memory alloys, Int. J. Plast. 129 (2020) 102686. doi:10.1016/j.ijplas.2020.102686.

[36] A. Sozinov, A. Soroka, N. Lanska, M. Rameš, L. Straka, K. Ullakko, Temperature dependence of twinning and magnetic stresses in Ni46Mn24Ga22Co4Cu4 alloy with giant 12% magnetic field-induced strain, Scr. Mater. 131 (2017) 33–36. doi:10.1016/j.scriptamat.2016.12.032.

[37] Y.J. He, H. Yin, R. Zhou, Q. Sun, Ambient effect on damping peak of NiTi shape memory alloy, Mater. Lett. 64 (2010) 1483–1486. doi:10.1016/j.matlet.2010.03.068.

[38] Y.J. He, Q.P. Sun, Rate-dependent domain spacing in a stretched NiTi strip, Int. J. Solids Struct. 47 (2010) 2775–2783. doi:10.1016/j.ijsolstr.2010.06.006.

[39] Y.J. He, Q.P. Sun, Frequency-dependent temperature evolution in NiTi shape memory alloy, Smart Mater. Struct. 19 (2010). doi:10.1088/0964-1726/19/11/115014.

[40] O.Z. Pascan, Y.J. He, Z. Moumni, W.H. Zhang, Temperature rise of high-frequency martensite reorientation via Type II twin boundary motion in NiMnGa Ferromagnetic Shape Memory Alloy, Scr. Mater. 104 (2015) 71–74. doi:10.1016/j.scriptamat.2015.04.006.
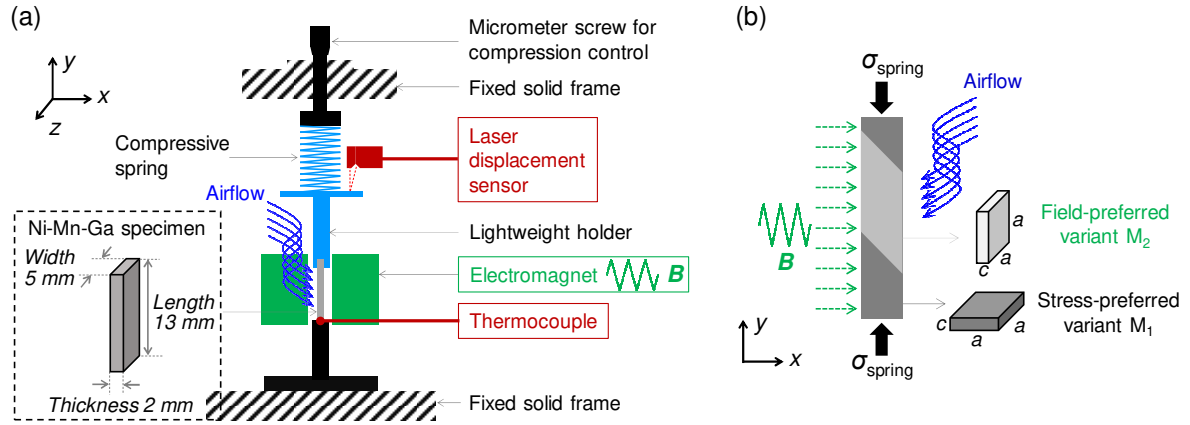
Figure 1. Schematics of (a) the experimental setup of the thermo-magneto-mechanical coupling actuation system and (b) the martensite reorientation of MSMA.
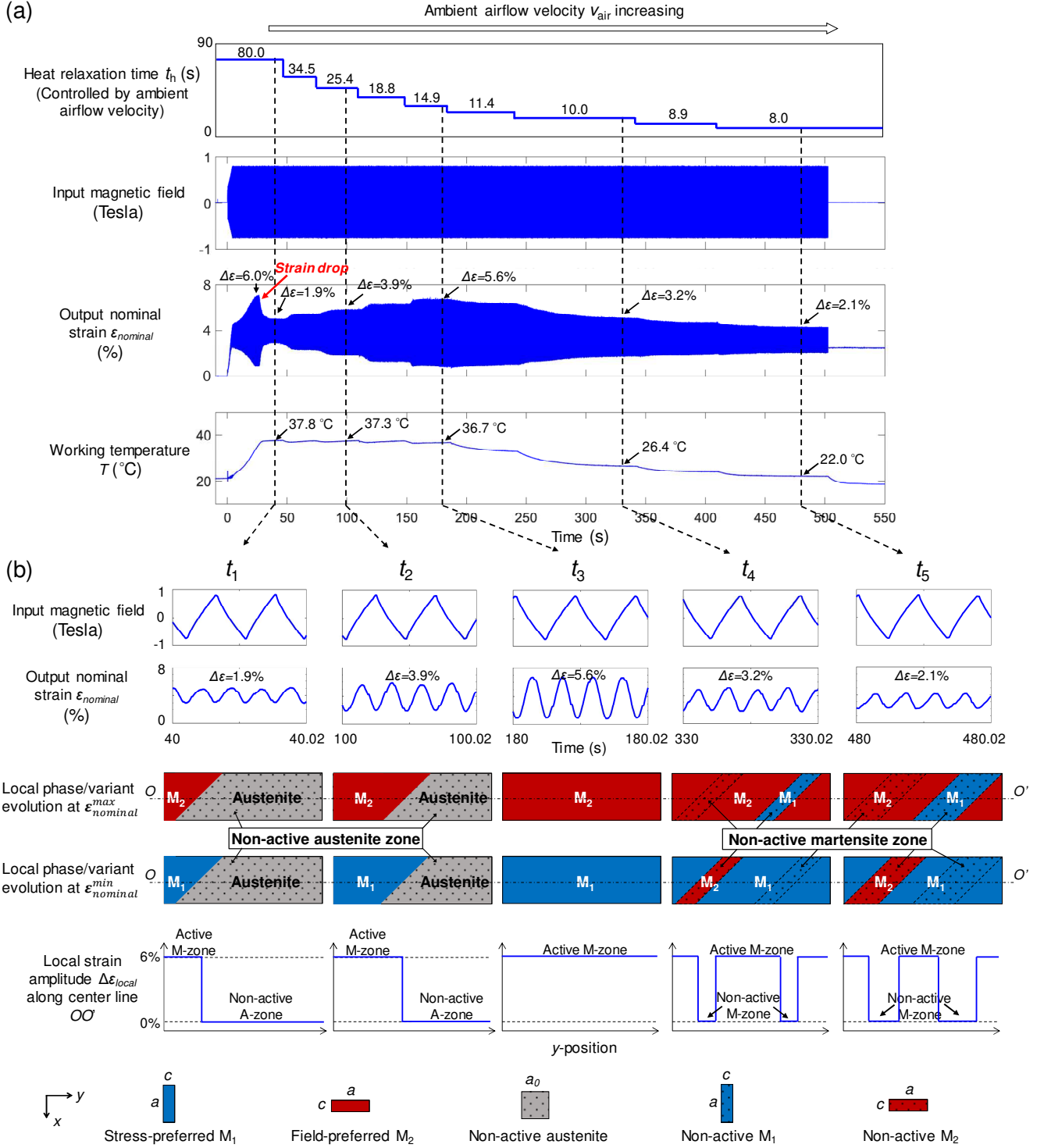
Figure 2. (a) The strain and temperature responses of MSMA under gradually increasing airflow velocity (i.e., gradually reducing the ambient heat relaxation time t_h); (b) the magnified views on the input magnetic field and the output strain evolutions and schematics of the local phase/variant evolutions at 5 typical time instants ($t_1 \sim t_5$).
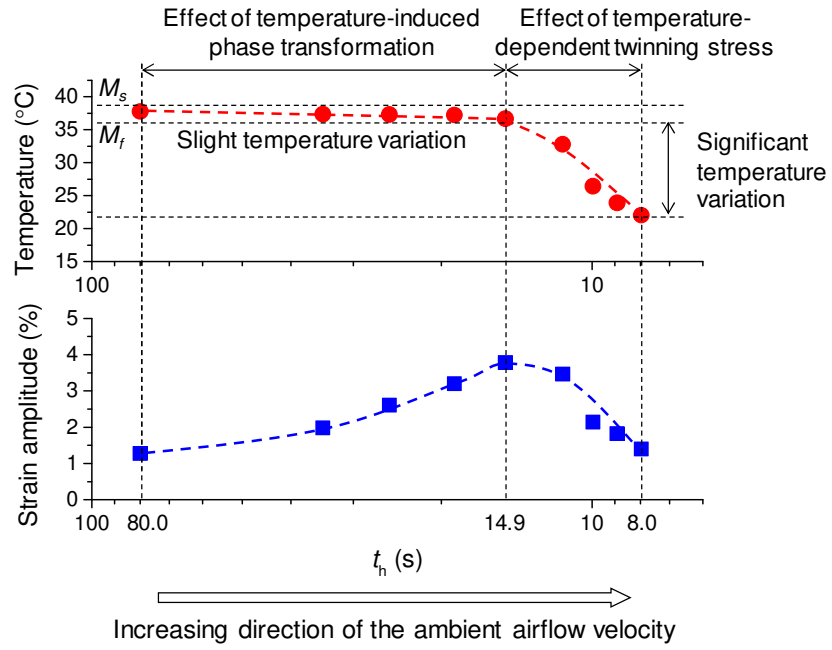
Figure 3. The dependence of the stable strain amplitude and the stable temperature of MSMA on the characteristic ambient heat relaxation time t_h. The dashed lines are for guiding eyes.
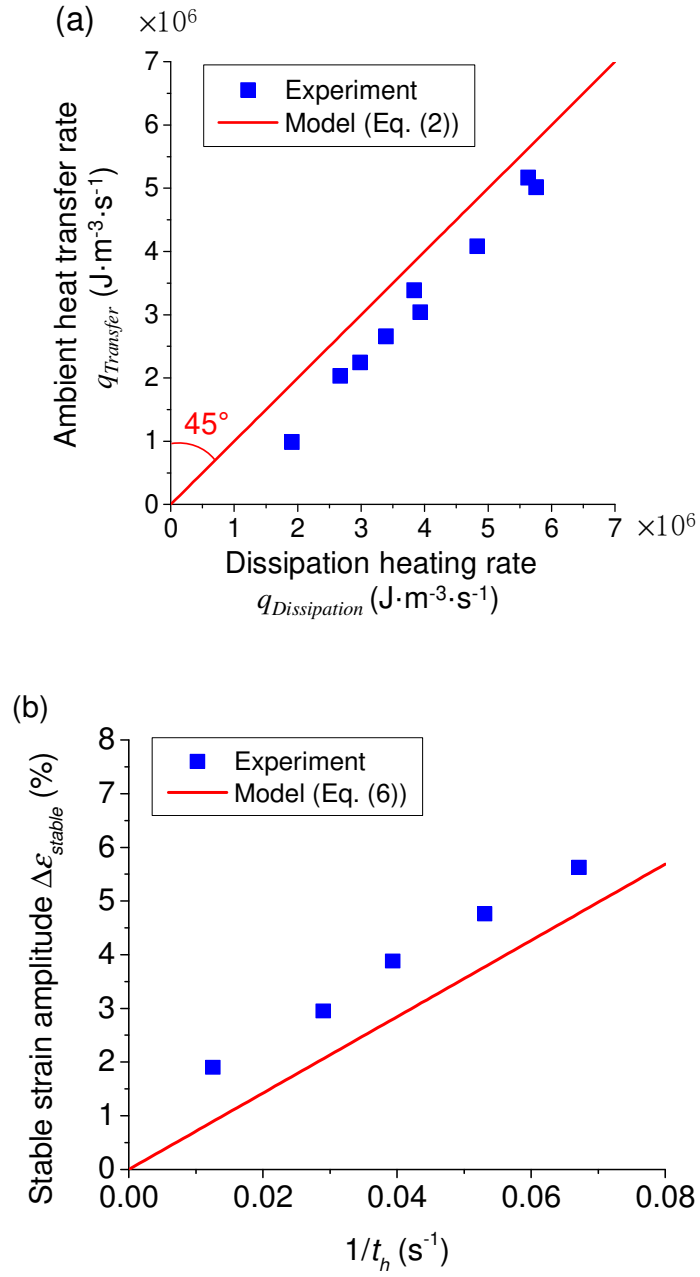
Figure 4. (a) Comparison between the experimental results and the heat balance model Eq. (2) (the red line); (b) Comparison of the strain amplitude $\Delta\varepsilon$ versus $1/t_h$ between experiment and theoretical model (Eq. (6)).
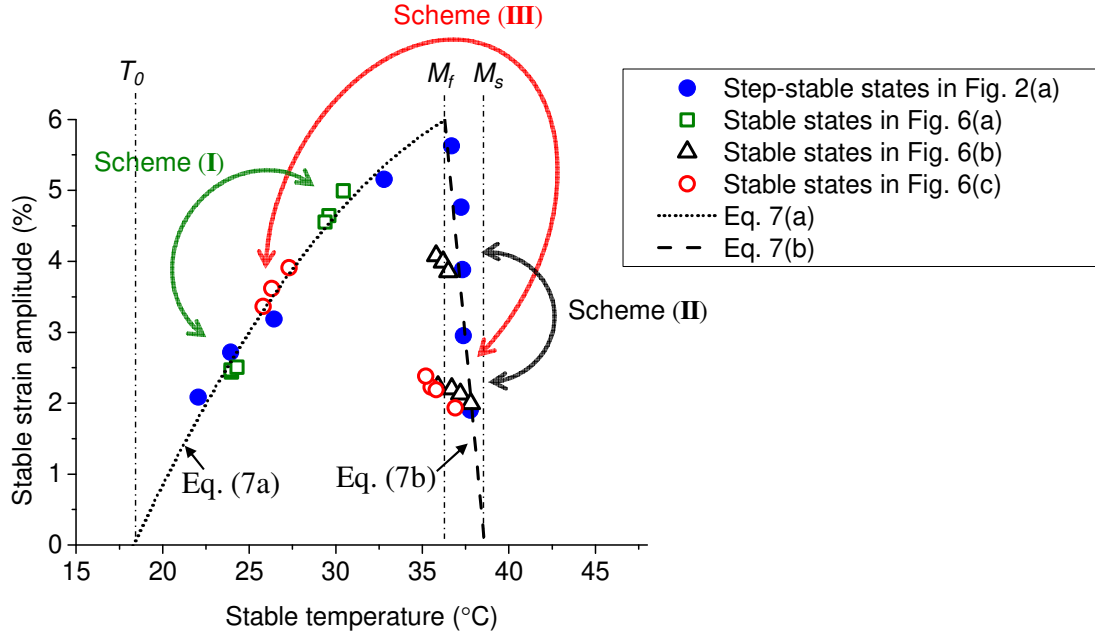
Fig. 5. The working states with certain relations between the stable strain amplitude and the stable temperature in a given magneto-mechanical loading condition (f_{mag}=110 Hz and σ_{ini}= 0.4 MPa) with varying ambient heat-transfer efficiency. The Eqs. 7(a) and 7(b) are respectively plotted as black dotted and dashed lines. The blue solid circles are from the step-stable states in Fig. 2(a); the green open squares, the black open triangles, and the red open circles are the results of the cyclic stable-state transitions of the Schemes (I), (II) and (III) as shown in Figs. 6(a), (b) and (c), respectively.

6(a) Scheme (I)

Heat relaxation time
t_h (s)

10.5

8.0

Input magnetic field
(Tesla)

1

0

-1

Output nominal strain
$\varepsilon_{nominal}$
(%)

10

0

$\Delta\varepsilon = 5.0$ $\Delta\varepsilon = 2.4$ $\Delta\varepsilon = 4.7$ $\Delta\varepsilon = 2.5$ $\Delta\varepsilon = 4.6$ $\Delta\varepsilon = 2.5$

Temperature T
(°C)

40

20

30.4   24.0   29.6   24.0   29.6   24.3

0   50   100   150   200   250   300   350

Time (s)

t_0^{stable} t_1^{switch} t_1^{stable} t_2^{switch} t_2^{stable} t_3^{switch} t_3^{stable} t_4^{switch} t_4^{stable} t_5^{stable} t_5^{stable}

t_1^{trans} t_2^{trans} t_3^{trans} t_4^{trans} t_5^{trans}

6(b) Scheme (II)

Heat relaxation time t_h (s)

Input magnetic field (Tesla)

Output nominal strain $\varepsilon_{nominal}$ (%)

$\Delta\varepsilon = 2.2$ $\Delta\varepsilon = 4.1$ $\Delta\varepsilon = 2.2$ $\Delta\varepsilon = 4.0$ $\Delta\varepsilon = 2.1$ $\Delta\varepsilon = 3.9$ $\Delta\varepsilon = 2.0$

Temperature T (°C)

35.9   35.8   36.7   36.2   37.2   36.5   37.8

Time (s)

t_0^{stable} t_1^{switch} t_1^{stable} t_2^{switch} t_2^{stable} t_3^{switch} t_3^{stable} t_4^{switch} t_4^{stable} t_5^{switch} t_5^{stable} t_6^{switch} t_6^{stable}

t_1^{trans} t_2^{trans} t_3^{trans} t_4^{trans} t_5^{trans} t_6^{trans}
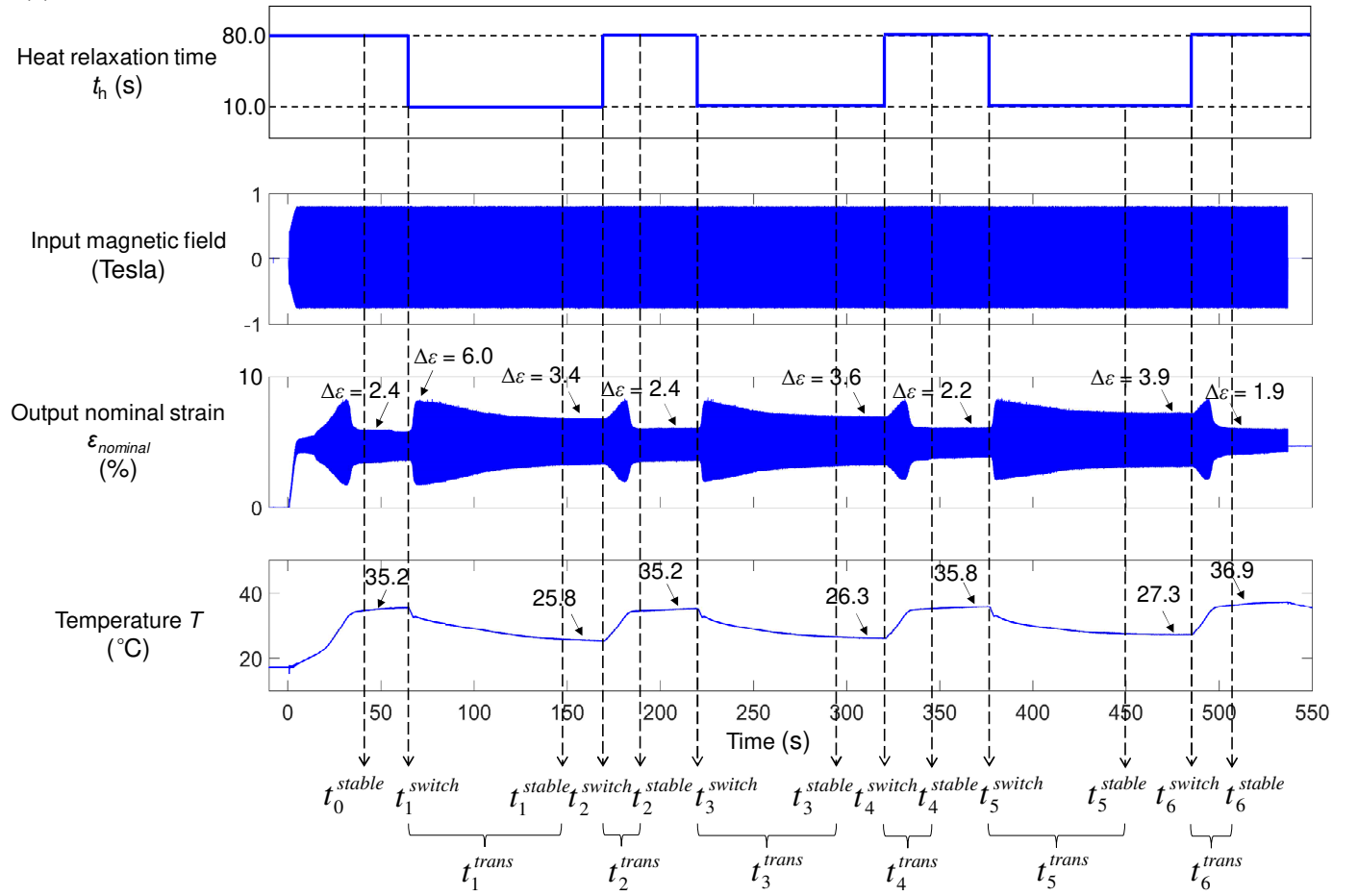
Figure 6. Cyclic transitions of different stable states driven by switching the ambient heat-transfer efficiency (a) Scheme (I) with cyclic switching t_h between 10.5 s and 8.0 s, (b) Scheme (II) with cyclic switching t_h between 80.0 s and 25.0 s, and (c) Scheme (III) with cyclic switching t_h between 80.0 s and 10.0 s.
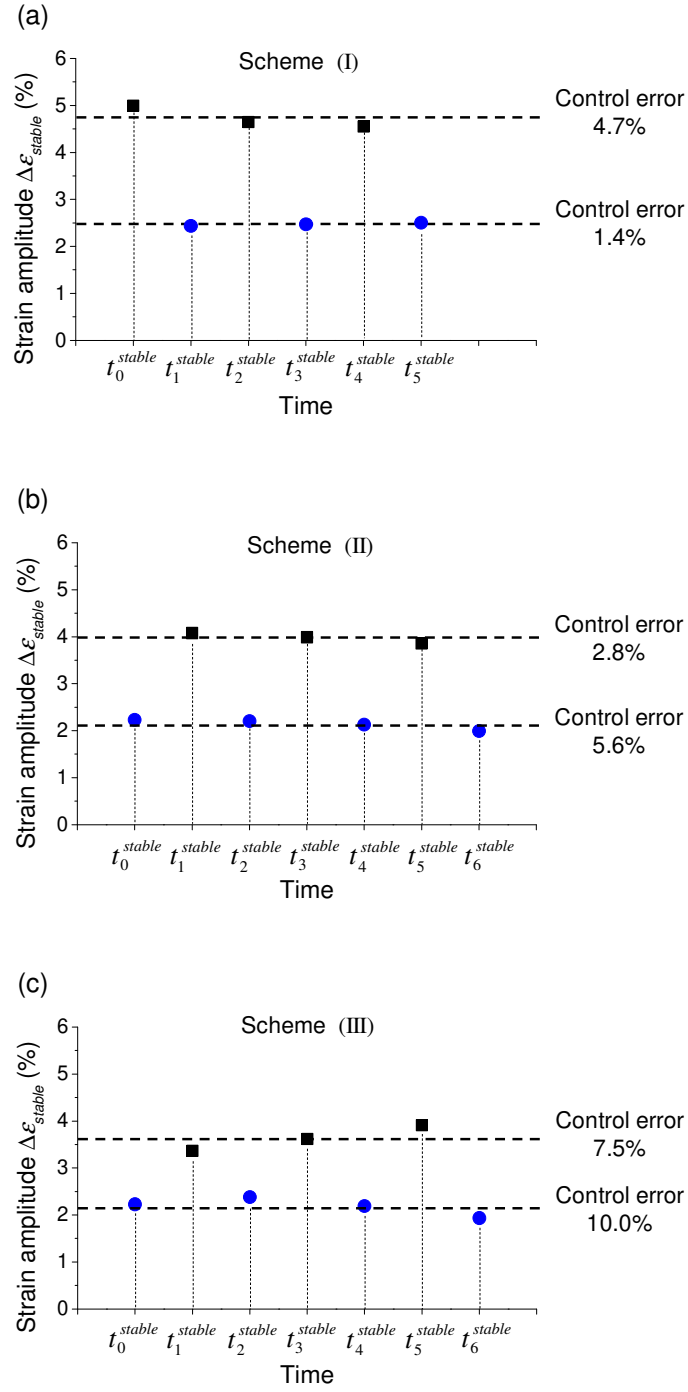
Figure 7. The strain amplitude scattering in Schemes I, II and III. The control error is defined as $\frac{\Delta\varepsilon^{max} - \Delta\varepsilon^{min}}{2\Delta\varepsilon^{mean}}$.

Table 1. The typical dynamic transition times in Schemes (I), (II) and (III).

Scheme	Transition time (s)					
	t_1^{trans}	t_2^{trans}	t_3^{trans}	t_4^{trans}	t_5^{trans}	t_6^{trans}
I	19	53	21	49	20	\
II	12	9	12	9	13	10
III	82	20	74	18	73	19

Appendix A

Determination of the characteristic heat-relaxation time t_h

To determine the characteristic heat-relaxation time t_h, the specimen is first heated by the actuation of a high-frequency cyclic martensite reorientation, then the applied magnetic field is turned off and the relaxation of the specimen temperature is measured in a constant ambient airflow. In this case the temperature relaxation is only determined by the heat convection. The value of the heat-relaxation time t_h is obtained by fitting the experimentally measured temperature relaxation data to an heat-convection relaxation equation [37,38]: $T = T_{\text{ambient}} + (T_{\text{initial}} - T_{\text{ambient}}) \cdot e^{-\frac{t}{t_h}}$ where T_{initial} is the specimen temperature at time $t = 0$ s. For example, by using this method, the value of t_h at the ambient airflow velocity of 0 m/s (i.e., ambient still air) is determined to be 80.0 s in Fig. A1. Similarly, t_h at different ambient conditions (different airflow velocity) can be experimentally measured.
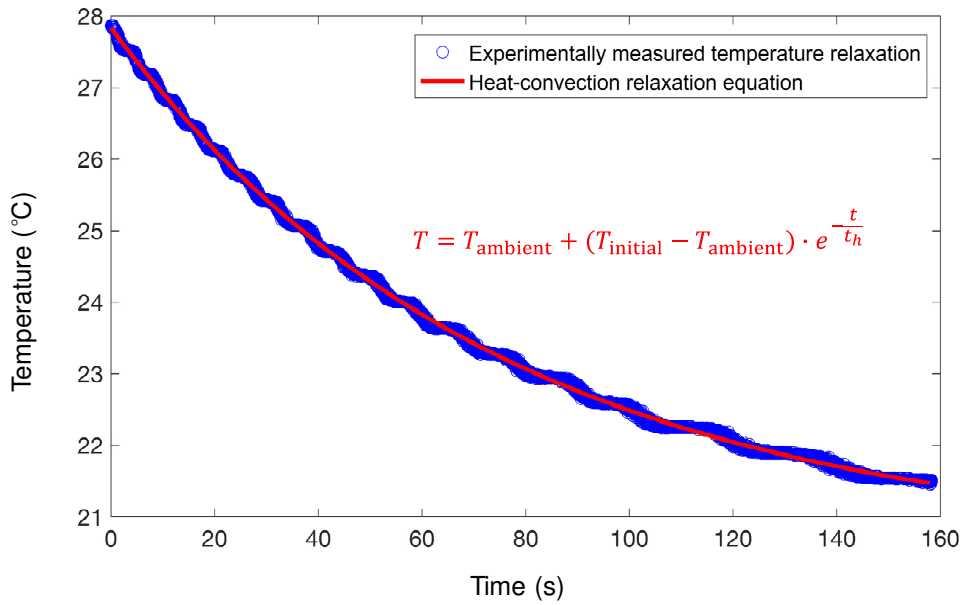

Figure A1. Measurement of the temperature relaxation time t_h of Ni-Mn-Ga single crystal specimen in still air ambient, where the characteristic heat-relaxation time t_h is fitted as 80.0 s.

Appendix B

One-dimensional heat balance model

The MSMA rectangular bar in this work can be approximately viewed as a one-dimensional (1D) bar with a diameter $2R$ as shown in Fig. B1, where the specimen temperature is assumed to be uniform and heated/cooled by the dissipation heat in the specimen and the heat transfer to the ambient respectively.
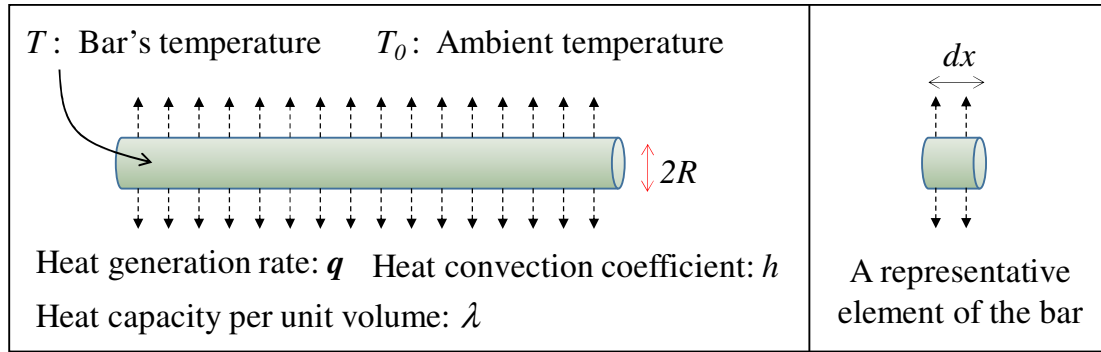

Figure B1. Schematic of the heat balance model of 1D bar.

For a representative element volume $dv = \pi R^2 \cdot dx$ where dx is the length of the element, the temperature variation is governed by the dissipation heat rate $q_{Dissipation}$ in the element volume and the heat convection via the element's surface area $dA = 2\pi R \cdot dx$ as

$$\lambda \cdot dv \cdot dT = q_{Dissipation} \cdot dv \cdot dt - h \cdot (T - T_0) \cdot dA \cdot dt \tag{B1}$$

where T, T_0, λ, and h denote the specimen temperature, the ambient temperature, the material heat capacity per unit volume, and the heat convection coefficient, respectively. Eq. (B1) can be reduced to

$$\frac{dT}{dt} = \frac{q_{Dissipation} - q_{Transfer}}{\lambda} \tag{B2}$$

where

$$q_{Transfer} = \frac{2h \cdot (T - T_0)}{R} \tag{B3}$$

When there is no dissipation heat generation (i.e., $q_{Dissipation} = 0$), Eq. (B2) reduces to

$$\frac{dT}{dt} = \frac{2h \cdot (T - T_0)}{R \cdot \lambda} \tag{B4}$$

whose solution is

$$T = T_0 + (T_{\text{initial}} - T_0) \cdot e^{-\frac{t}{t_h}} \tag{B5}$$

where T_{initial} denote the specimen temperature at $t = 0$ second, and

$$t_h = \frac{R\lambda}{2h} \tag{B6}$$

Equation (B5) and (B6) provide the method to characterize the ambient heat-transfer efficiency in Appendix A. With Eq. (B6), Eq. (B3) can be written as

$$q_{Transfer} = \frac{\lambda \cdot (T - T_0)}{t_h} \tag{B7}$$

where all the parameters/variables are measurable.

When there is the heat generation of the martensite reorientation, the heat generation rate $q_{Dissipation}$ is non-zero and can be written as

$$q_{Dissipation} = 2\sigma_{tw} \cdot \Delta\varepsilon \cdot f_{strain} \tag{B8}$$

where σ_{tw}, $\Delta\varepsilon$, and f_{strain} represent the effective twinning stress of the martensite reorientation, the strain amplitude and the strain frequency, respectively. So, Eqs. (B2), (B8) and (B7) are used in the discussion of Section 3.2, corresponding to Eqs. 1(a), 1(b) and 1(c) respectively.